

# Cubic AgMnSbTe<sub>3</sub> semiconductor with a high thermoelectric performance

Yubo Luo,<sup>†</sup> Tian Xu,<sup>†</sup> Zheng Ma,<sup>†</sup> Dan Zhang,<sup>#</sup> Zhongnan Guo,<sup>‡</sup> Qinghui Jiang,<sup>†</sup> Junyou Yang,<sup>†,\*</sup> Qingyu Yan,<sup>‡,\*</sup> Mercouri G. Kanatzidis<sup>§,\*</sup>

<sup>†</sup>State Key Laboratory of Materials Processing and Die & Mold Technology, School of Materials Science and Engineering, Huazhong University of Science and Technology, Wuhan, 430074, P. R. China

<sup>‡</sup>School of Materials Science and Engineering, Nanyang Technological University, 50 Nanyang Avenue, Singapore 639798, Singapore

<sup>§</sup>Department of Chemistry, Northwestern University, Evanston, Illinois 60208, USA

<sup>#</sup>College of Physics Science and Technology, Hebei University, Baoding, 071002, P. R. China

**KEYWORDS.** *AgSbTe<sub>2</sub>, thermoelectric, high entropy, thermal conductivity, AgMnSbTe<sub>3</sub>*

**ABSTRACT:** The reaction of MnTe with AgSbTe<sub>2</sub> in an equimolar ratio (ATMS) provides a new semiconductor, AgMnSbTe<sub>3</sub>. AgMnSbTe<sub>3</sub> crystallizes in an average rock-salt NaCl structure with Ag, Mn, and Sb cations statistically occupying the Na sites. AgMnSbTe<sub>3</sub> is a *p*-type semiconductor with a narrow band gap of ~0.33 eV. A pair distribution function analysis indicates that local distortions are associated with the location of the Ag atoms in the lattice. Density functional theory calculations suggest a specific electronic band structure with multi-peak valence band maxima prone to energy convergence. In addition, Ag<sub>2</sub>Te nanograins precipitate at grain boundaries of AgMnSbTe<sub>3</sub>. The energy offset of the valence band edge between AgMnSbTe<sub>3</sub> and Ag<sub>2</sub>Te is ~0.05 eV, which implies that Ag<sub>2</sub>Te precipitates exhibit a negligible effect on the hole transmission. As a result, ATMS exhibits a high power factor of ~12.2  $\mu\text{Wcm}^{-1}\text{K}^{-2}$  at 823 K, ultralow lattice thermal conductivity of ~0.34  $\text{Wm}^{-1}\text{K}^{-1}$  (823 K), high peak *ZT* of ~1.46 at 823 K, and high average *ZT* of ~0.87 in the temperature range of 400–823 K.

## ■ INTRODUCTION

The thermoelectric technology can directly convert heat into electrical power and can enable energy savings by efficiently harvesting and managing waste heat.<sup>1</sup> Therefore, thermoelectric power generator prototypes have been intensively explored in recent years,<sup>2</sup> involving many thermoelectric materials, such as Bi<sub>2</sub>Te<sub>3</sub>,<sup>3</sup> PbTe,<sup>4,5</sup> Mg<sub>2</sub>Si,<sup>6,7</sup> half-Heusler<sup>8</sup> and GeTe.<sup>9</sup> To enable their widespread deployment, high energy conversion efficiencies  $\eta$  of thermoelectric modules and thus high thermoelectric figures of merit *ZT* of the employed materials are required. *ZT* is defined as  $ZT = S^2\sigma T/(\kappa_e + \kappa_L)$ , where *S*,  $\sigma$ ,  $\kappa_e$ ,  $\kappa_L$ , and *T* are the Seebeck coefficient, electrical conductivity, electronic thermal conductivity, lattice thermal conductivity, and absolute temperature, respectively. The major challenge in enhancing *ZT* is to decouple the physical contraindicated interrelationship of *S*,  $\sigma$ , and  $\kappa_e$ . Over the past two decades, through theoretical and technological innovations, superior *ZT* values have been obtained for several systems, such as PbTe,<sup>10</sup> PbSe,<sup>11</sup> GeTe,<sup>12-13</sup> AgSbTe<sub>2</sub>,<sup>14-15</sup> Cu<sub>2</sub>Se,<sup>16</sup> SnSe,<sup>17-19</sup> CuInTe<sub>2</sub>,<sup>20-21</sup> and half-Heusler alloys.<sup>22</sup> Recently, entropy engineering of such materials<sup>23-24</sup> has been used to stabilize higher-symmetry crystal structures in thermoelectric materials (e.g., GeSe,<sup>25</sup> SnSe,<sup>26</sup> GeTe,<sup>27</sup> AgSnSbSe<sub>3</sub><sup>28</sup>). The entropy engineering also reduces the lattice thermal conductivity owing to the strengthened lattice distortion,

atomic mass fluctuation, point defects, and other crystallographic defects.<sup>29-30</sup>

MnTe is a *p*-type chalcogenide semiconductor with a direct band gap of 1.3 eV and indirect band gap of 0.8 eV at room temperature, which has attracted increasing attention among the thermoelectric community as a lead-free alternative.<sup>31-32</sup> However, the low electrical conductivity of pristine MnTe owing to its low carrier concentration (~10<sup>18</sup> cm<sup>-3</sup>) and low hole mobility (~6 cm<sup>2</sup>V<sup>-1</sup>s<sup>-1</sup>) severely restricts its thermoelectric performance, with a *ZT* value of only ~0.5 at 823 K.<sup>33</sup> Therefore, it is of interest to enhance its electrical conductivity through substitution of monovalent metals (e.g., Ag,<sup>32</sup> Cu,<sup>34</sup> Li,<sup>35</sup> Na<sup>36</sup>) for Mn and incorporation of inclusions with high electrical conductivities (e.g., SnTe,<sup>37</sup> Ag<sub>2</sub>S,<sup>38</sup> Graphene,<sup>39</sup> Sb<sub>2</sub>Te<sub>3</sub>).<sup>40</sup> Generally, MnTe crystallizes in a hexagonal crystal structure with a space group of *P6<sub>3</sub>/mmc* (No. 194). However, it can also crystallize in the cubic NaCl structure under specific preparation methods. For example, cubic MnTe films can be obtained on (001) GaAs substrates by molecular beam epitaxy<sup>41</sup> or on a cleaved sodium chloride by vapor deposition.<sup>42</sup>

In this study, we introduce a direct route to stabilize cubic MnTe by entropy-driven alloying of AgSbTe<sub>2</sub>. AgSbTe<sub>2</sub> exhibits a rock-salt crystal structure with a space group of *Fm-3m* (No. 225) and ultrahigh *ZT* of ~1.5 at room temperature and ~2.6 at 573 K by cadmium doping (i.e., AgSb<sub>0.94</sub>Cd<sub>0.06</sub>Te<sub>2</sub>).<sup>15</sup> AgMn<sub>*m*</sub>SbTe<sub>*m+2*</sub> (*m* =

1–10) samples (i.e., MnTe matrix and 5–50% AgSbTe<sub>2</sub>) were synthesized by melting and quenching (see experimental section in the Supporting information for details). Phase and microstructure analyses show that the sample with  $m = 1$  (AgMnSbTe<sub>3</sub>), i.e., the equimolar mixture of AgSbTe<sub>2</sub> and MnTe, is composed of AgMnSbTe<sub>3</sub> (main phase) and Ag<sub>2</sub>Te (impurity). To distinguish the AgMnSbTe<sub>3</sub> sample from the proper AgMnSbTe<sub>3</sub> compound, we refer to the AgMnSbTe<sub>3</sub> sample as antimony tellurium manganese silver (ATMS). The AgMnSbTe<sub>3</sub> compound exhibits the same rock-salt structure. Density functional theory (DFT) calculations suggest that it is a narrow-band-gap semiconductor with a specific electronic structure with multiple valence band peaks near the Fermi energy. These features result in superior electrical transport properties in ATMS, including a power factor of  $12.2 \mu\text{Wcm}^{-1}\text{K}^{-2}$  at 823 K, compared to  $5.4 \mu\text{Wcm}^{-1}\text{K}^{-2}$  for MnTe at 823 K and  $8.5 \mu\text{Wcm}^{-1}\text{K}^{-2}$  for AgSbTe<sub>2</sub> at 723 K. The unique composite arrangement combined with local distortion created by disordered Ag, Mn, and Sb cations strengthens the phonon scattering in ATMS, resulting in an ultralow lattice thermal conductivity of  $\sim 0.34 \text{ Wm}^{-1}\text{K}^{-1}$  at 823 K. The superior electrical and thermal transport properties to those of MnTe provide a peak  $ZT$  of  $\sim 1.46$  at 823 K for ATMS combined with a high average  $ZT$  of  $\sim 0.87$  (400–823 K), thus a high potential for thermoelectric power generation.

## RESULTS AND DISCUSSION

### 1. Phase formation, crystal structure, and microstructure

We prepared the AgMn<sub>*m*</sub>SbTe<sub>*m*+2</sub> ( $m=1, 2, 4, 6, 10$ ) series of samples by melting stoichiometric quantities of elemental Ag, Mn, Sb, and Te at 1173 K for 20 h followed by water quenching (see experimental section in the Supporting Information for details). Figure 1A shows powder X-ray diffraction (PXRD) patterns of MnTe and AgMn<sub>*m*</sub>SbTe<sub>*m*+2</sub> ( $m = 1, 2, 4, 6, \text{ and } 10$ ). The Bragg peaks of MnTe are indexed to the NiAs structure with hexagonal symmetry ( $P6_3/mmc$ ). With the AgSbTe<sub>2</sub> alloying, new Bragg peaks at 29.6, 30.2, 60.8, and 70.0° emerged, which belong to the rock salt structure. For  $m = 1$  (i.e., ATMS), all Bragg peaks belong to that rock salt structure, while the peaks of MnTe are undetectable. Rietveld refinement (Figure 1B) on the PXRD pattern of ATMS yielded a cubic cell parameter  $a = 6.0198(4) \text{ \AA}$ , smaller than that of AgSbTe<sub>2</sub> ( $a = 6.0677(9) \text{ \AA}$ )<sup>43</sup> owing to the smaller atomic radius of Mn (1.32 Å) than those of Ag (1.44 Å) and Sb (1.60 Å). In this cubic structure, the Ag, Mn, and Sb cations are believed to be statistically disordered at the (0.5, 0.5, 0.5) sites in an ideal structure (Figure S1, Supporting Information). This indicates that the hexagonal MnTe can be destabilized and converted to a cubic structure, presumably by entropy-driven alloying of the equimolar fraction of AgSbTe<sub>2</sub> to form a new phase of AgMnSbTe<sub>3</sub>. Such a chemical modification route was also used to convert GeSe<sup>25</sup> and SnSe<sup>26</sup> to a NaCl structure by the entropy-driven alloying of AgBiSe<sub>2</sub> and AgSbSe<sub>2</sub>, respectively. In addition, according to the Rietveld refinement, a small amount of Ag<sub>2</sub>Te ( $\sim 3 \text{ mol\%}$ ) was indexed in the PXRD of ATMS, which is often observed in AgSbTe<sub>2</sub>-based materials.<sup>44–45</sup> The presence of Ag<sub>2</sub>Te was confirmed by transmission electron microscopy (TEM), as discussed below.

In addition, the Bragg peaks of MnTe and rock-salt AgMnSbTe<sub>3</sub> simultaneously exist for the samples with  $m = 2, 4, 6, \text{ and } 10$ , without Bragg peak shift of MnTe and AgMnSbTe<sub>3</sub>

compared to that of the MnTe and ATMS samples, which implies that these materials are a mixture of MnTe and AgMnSbTe<sub>3</sub>. Our Rietveld refinements show that the cell parameters of AgMnSbTe<sub>3</sub> are similar for the samples with  $m = 2, 4, 6, \text{ and } 10$ ; the cell parameters of MnTe are also similar (Table S1 in the Supporting Information). Therefore, a single AgMnSbTe<sub>3</sub> can only be formed when MnTe and AgSbTe<sub>2</sub> react in an equimolar ratio. To better analyze this new compound, AgMnSbTe<sub>3</sub>, we mainly focused on the microstructure, electronic structure, and thermoelectric performance of ATMS.

We performed a synchrotron X-ray total scattering analysis using the atomic pair distribution function (PDF) analysis technique at 300 K to understand the crystal structure of AgMnSbTe<sub>3</sub>. The long-range X-ray PDF peaks (e.g., with  $r$  of 14–28 Å) of AgMnSbTe<sub>3</sub> fit well with the cubic rock-salt structure model (Figure S1), which was refined to a weighted  $R_w$  value of  $\sim 7.9 \%$  (Figure 1C). However, the short-range X-ray PDF peaks (with  $r$  of 2.5–5.0 Å) had a poor fit with the cubic rock-salt structure, with  $R_w$  as high as 15.1%. The good fit in the long range and poor fit in the short range indicate local non-periodic lattice distortion in the cubic AgMnSbTe<sub>3</sub>. Therefore, we used a distorted model shown in Figure 1E to fit the short-range X-ray PDF peaks (2.5–5.0 Å) and obtained a reasonable description of the local distortion with  $R_w = 4.7 \%$  (see Figure 3F). The distorted model requires off-centering of the Ag atoms toward the  $\langle 100 \rangle$  direction with a displacement of  $\sim 0.12 \text{ \AA}$  under  $P1$  symmetry (cell parameters:  $a = 5.996(5) \text{ \AA}$ ,  $b = 5.776(2) \text{ \AA}$ ,  $c = 6.278(3) \text{ \AA}$ ,  $\alpha = \beta = \gamma = 90^\circ$ ). The off-centering of the Ag atoms leads to statistical disorder along all possible  $\langle 100 \rangle$  directions, as observed in Sn<sub>1-x</sub>Ge<sub>x</sub>Te,<sup>46</sup> AgPbBiSe<sub>3</sub>,<sup>47</sup> Ge<sub>2</sub>Sb<sub>2</sub>Te<sub>5</sub>,<sup>48</sup> and PbSe,<sup>49–50</sup> and is expected to contribute to the low lattice thermal conductivity of AgMnSbTe<sub>3</sub>.

To understand the microstructure of ATMS, we performed a back-scattered electron (BSE) imaging analysis using scanning electron microscopy to investigate the polished surface of the ATMS sample. The BSE image (Figure 2A) shows that ATMS is composed of two phases. The corresponding chemical compositions were analyzed by energy-dispersive X-ray spectroscopy (Figure 2B). The main phase (dark contrast) was the AgMnSbTe<sub>3</sub> compound, whose grain size is tens of micrometers; while Ag<sub>2</sub>Te was a secondary phase (light contrast), distributed dispersedly at the grain boundaries of AgMnSbTe<sub>3</sub> with nanoscale grain sizes (Figure S2 in the Supporting Information).

Furthermore, we performed scanning transmission electron microscopy–energy-dispersive X-ray spectroscopy (STEM-EDS) elemental mapping of ATMS (Figure 2C, D), which revealed that Ag, Mn, Sn, and Te were distributed uniformly throughout the AgMnSbTe<sub>3</sub> grains. In addition, submicron precipitates were observed at the grain boundaries of AgMnSbTe<sub>3</sub> (Figure 2E). Clear lattice fringes of the precipitate are observed in the high-resolution TEM image (Figure 2F). The corresponding fast Fourier transform pattern of the precipitate is presented in the inset of Figure 2F. The bright dots of the pattern can be indexed to the (102), (213), and (111) planes of the monoclinic Ag<sub>2</sub>Te along its [211] zone axis. Therefore, our XRD, BSE, and STEM-EDS results confirm that ATMS is composed of microscale AgMnSbTe<sub>3</sub> and nanoscale Ag<sub>2</sub>Te gathered at the grain boundaries of AgMnSbTe<sub>3</sub>.

## 2. Electronic band structure of AgMnSbTe<sub>3</sub>

We performed first-principle DFT calculations on the special quasi-random structure (SQS, Figure S3 in the Supporting Information)<sup>51–52</sup> of AgMnSbTe<sub>3</sub>, because the standard DFT calculations are not directly applicable to random alloys expressed by average occupancies of constituent atoms.<sup>53</sup> The SQS leads to the best periodic supercell approximation for a truly disordered state, which can mimic the electronic properties of disordered systems to a reasonable extent, thus is widely used to assess the electronic structure of disordered solid solution systems.<sup>54</sup> The SQS structure of AgMnSbTe<sub>3</sub> is different from the distorted one shown in Figure 1E and average rock salt structure shown in Figure S1.<sup>55</sup> Additional details for these calculations are provided in the Supporting Information. Considering that the Mn<sup>2+</sup> centers are paramagnetic with a  $d^5$  electronic configuration, Figure 3a and 3b show the calculated spin-up and spin-down electronic band structures of AgMnSbTe<sub>3</sub>, respectively. The Fermi level is at 0 eV in both cases to separate the valence band maximum (VBM) from the conduction band minimum (CBM). The absence of electronic state in both spin channels at the Fermi level reflects the semiconductor structure of AgMnSbTe<sub>3</sub>, which has a direct band gap of ~0.10 eV in the spin-up channels and indirect band gap of ~0.12 eV in the spin-down channels. The DFT calculations under-estimated the band gap of AgMnSbTe<sub>3</sub>, which is lower than the measured optical band gap (~0.36 eV, Figure S4).

Notably, the calculations indicate that AgMnSbTe<sub>3</sub> has a complex multiple-peak valence band structure. For the spin-up channels, the first and second VBMs are located at the Q and F points, respectively, and there is third VBM along the Q–Z direction with an energy difference between the first and third VBM of ~0.07 eV. For the spin-down channels, the first VBM is located at point F, the second and third VBMs are along the Q–Z and Q–F directions, respectively, and the energy difference between the first and third VBM is ~0.06 eV. Such small energy differences are promising for multiple valence band convergence resulting (upon hole doping) in high Seebeck coefficient and power factor, as observed for other thermoelectric materials.<sup>56–57</sup>

The total density of states (DOS) (Figure 3C) reveals similar results, as for the electronic band structure profile, with the Fermi level remaining in the gap in both spin-up and spin-down states, indicating its semiconducting structure. The total DOS also shows a slight difference between the spin-up and spin-down states, particularly near the Fermi level. This difference is attributed mainly to the difference in Mn 3d for spin-up and spin-down channels, as shown by the partial densities of states in Figure 3D. In addition, the main valence band peaks around the Fermi level in both spin-up and spin-down states originate from the strong hybridization between Ag 4d, Mn 3d, Sb 5p, and Te 5p orbitals.

Figure 3E shows ultraviolet photoelectron spectroscopy spectra of AgMnSbTe<sub>3</sub> and Ag<sub>2</sub>Te measured at 300 K. The onset edge values of AgMnSbTe<sub>3</sub> and Ag<sub>2</sub>Te are estimated to be 0.10 and 0.25 eV, while the cutoff edge values of AgMnSbTe<sub>3</sub> and Ag<sub>2</sub>Te are estimated to be 17.3 and 17.4 eV, extracted from the ultraviolet photoelectron spectroscopy spectra, respectively. Therefore, the valence band values of AgMnSbTe<sub>3</sub> and Ag<sub>2</sub>Te are -4 and -4.05 eV, respectively. Thus, the energy offset of the valence band between AgMnSbTe<sub>3</sub> and Ag<sub>2</sub>Te is only 0.05 eV

(Figure 3F), which shows a good band alignment between AgMnSbTe<sub>3</sub> and Ag<sub>2</sub>Te. This implies a “barrier-free access” for hole transmission between these two phases.

## 3. Thermoelectric performance

Figure 4 shows the thermoelectric properties of AgMn<sub>m</sub>SbTe<sub>m+2</sub>, ( $m = 1, 2, 4, 6$ , and  $10$ ), along with those of MnTe and AgSbTe<sub>2</sub> for comparison. As mentioned above, MnTe has a low electrical conductivity of ~7.1 S/cm at room temperature owing to its low hole concentration and mobility. The poor electrical conductivity is largely enhanced by the AgSbTe<sub>2</sub> alloying and reaches ~158.4 S/cm at room temperature for ATMS. Hall coefficient measurements (see experimental section in the Supporting Information for details) reveal that the increase in electrical conductivity is attributed to the simultaneous enhancements in Hall carrier concentration (e.g.,  $\sim 1.5 \times 10^{19} \text{ cm}^{-3}$ ) and mobility ( $64 \text{ cm}^2 \text{ V}^{-1} \text{ s}^{-1}$ ) of ATMS. The observed enhancement in mobility is very important for the thermoelectric community, as point defect engineering and nanostructuring commonly result in a reduction in mobility. We attribute the enhancement in the mobility of MnTe to the large change in the electronic band structure by the AgSbTe<sub>2</sub> alloying, resulting in a smaller band effective mass in ATMS. In addition, the high mobility implies that the highly ordered Te atoms over the Cl sites of the NaCl lattice are conducive to the maintenance of a high electric conductivity in AgMnSbTe<sub>3</sub>, although its cations are highly disordered.<sup>48</sup>

The electrical conductivity of ATMS exhibits a heavily doped semiconductor behavior in the temperature range of 300–623 K, which is reduced from 158.4 S/cm at ~300 K to a minimum value of 91.1 S/cm at 623 K. It then increases to 242 S/cm at 823 K with the further increase in temperature, owing to the well-known intrinsic excitation for narrow-band-gap semiconductors. In addition, the AgMn<sub>m</sub>SbTe<sub>m+2</sub> samples with  $2 \leq m \leq 10$  are mixtures of MnTe and AgMnSbTe<sub>3</sub>, as reflected by the XRD pattern. Thus, the electrical conductivity increases with the decrease in  $m$  as a consequence of the increasing amount of the AgMnSbTe<sub>3</sub> phase.

The Seebeck coefficients (Figure 4B) of AgMn<sub>m</sub>SbTe<sub>m+2</sub> ( $m = 1, 2, 4, 6$ , and  $10$ ) are positive, which implies that holes are the majority carriers in these samples, in good agreement with the Hall measurements. The Seebeck coefficients decrease with the decrease in  $m$  as a result of the increase in the amount of AgMnSbTe<sub>3</sub>, i.e., hole concentration, as shown in Table S2 in the Supporting Information. ATMS has the lowest Seebeck coefficient, which increases from ~197  $\mu\text{V/K}$  at 300 K to a maximum value of ~289  $\mu\text{V/K}$  at 573 K and exhibits a heavily doped semiconductor behavior. The Seebeck coefficient then decreases to ~225  $\mu\text{V/K}$  at 823 K owing to the intrinsic excitation (i.e., bipolar carrier diffusion). We estimated the Goldsmid–Sharp band gap of ATMS using  $E_{\text{gs}} = 2e|S|_{\text{max}}T_{\text{max}}$ , where  $T_{\text{max}}$  is the temperature at which the Seebeck coefficient is maximized at  $S_{\text{max}}$ .<sup>58</sup>  $E_{\text{gs}}$  is estimated to be ~0.33 eV, very close to the optical value obtained using Fourier-transform infrared spectroscopy (~0.36 eV, Figure S4).

The power factor  $S^2\sigma$  of AgMn<sub>m</sub>SbTe<sub>m+2</sub> ( $m = 1, 2, 4, 6$ , and  $10$ ) increases with the decrease in  $m$ , as shown in Figure 4C. ATMS has the highest power factor in the system, which increases from ~6.1  $\mu\text{Wcm}^{-1}\text{K}^{-2}$  at ~300 K to 12.2  $\mu\text{Wcm}^{-1}\text{K}^{-2}$  at



823 K. The average power factors of MnTe and AgMnSbTe<sub>3</sub> are ~2.4 and ~8.5  $\mu\text{Wcm}^{-1}\text{K}^{-2}$  in the temperature range of 400 to 823 K respectively, which shows an increase of ~254%.

Figure 4D shows the thermal conductivities of AgMn<sub>m</sub>SbTe<sub>m+2</sub> ( $m = 1, 2, 4, 6$ , and 10) and MnTe for comparison. The thermal conductivity of MnTe increases from ~1.2  $\text{Wm}^{-1}\text{K}^{-1}$  at ~300 K to 1.38  $\text{Wm}^{-1}\text{K}^{-1}$  at ~323 K owing to the transition between antiferromagnetism to para-ferromagnetism.<sup>35-36</sup> Similar tendencies are observed for the samples with  $m = 10$  and  $m = 6$  with dominant MnTe. With the further increase in the content of AgMnSbTe<sub>3</sub>, e.g., at  $m = 4, 2$ , and 1, such tendency disappears. ATMS exhibits a low thermal conductivity of ~0.7  $\text{Wm}^{-1}\text{K}^{-1}$  at 300 K, ~40% lower than that (~1.2  $\text{Wm}^{-1}\text{K}^{-1}$ ) of MnTe. With the increase in temperature, the thermal conductivity of ATMS decreases to 0.57  $\text{Wm}^{-1}\text{K}^{-1}$  at 623 K. Figure 4E shows the lattice thermal conductivities of the AgMn<sub>m</sub>SbTe<sub>m+2</sub> samples obtained by extracting the electronic thermal conductivity  $\kappa_e$  (Figure S5 in the Supporting Information), which was estimated using the Wiedemann–Franz relation,  $\kappa_e = L\sigma T$ . The temperature-dependent Lorentz number,  $L$ , was estimated by the measured Seebeck coefficient according to a semi-empirical equation,  $L = 1.5 + \exp(-S/116)$ .<sup>59</sup> The lattice thermal conductivity of AgMn<sub>m</sub>SbTe<sub>m+2</sub> decreases with the decrease in  $m$ , i.e., ATMS exhibits the lowest lattice thermal conductivity in the system, which is only slightly higher than that of AgSbTe<sub>2</sub>. At 300 K, the lattice thermal conductivity of ATMS is ~0.62  $\text{Wm}^{-1}\text{K}^{-1}$ , compared to 0.55  $\text{Wm}^{-1}\text{K}^{-1}$  for AgSbTe<sub>2</sub> and ~1.2  $\text{Wm}^{-1}\text{K}^{-1}$  for pristine MnTe. The low value continually decreases to ~0.34  $\text{Wm}^{-1}\text{K}^{-1}$  at 823 K, which is among the lowest values for well-known thermoelectric semiconductors (e.g., InTe,<sup>60</sup>  $\alpha$ -Cu<sub>2</sub>Se,<sup>61</sup> SnSe,<sup>19, 62</sup> and Ag<sub>8</sub>SnSe<sub>6</sub>).<sup>63</sup> We attribute the ultralow lattice thermal conductivity in ATMS to the synergy of local distortion of Ag, high anharmonicity, and high cation disorder in the lattice. Notably, the level of phonon scattering at the AgMnSbTe<sub>3</sub>/Ag<sub>2</sub>Te interface is more challenging to assess because these precipitates are generally large (hundreds of nanometers) and occur sparsely in the grain boundaries of the sample. The strong phonon scattering in ATMS is also reflected in the mean sound velocity of 1792 m/s at room temperature (see experimental section in the Supporting Information for details), which is lower than those of PbS (2128 m/s), SnTe (2066 m/s), GeTe (2190 m/s), InSb (2062 m/s), FeNbSb (3473 m/s) and PbSe (1963 m/s).<sup>63</sup>

Figure 4F shows the thermoelectric performances of AgMn<sub>m</sub>SbTe<sub>m+2</sub> ( $m = 1, 2, 4, 6$ , and 10). The high power factor and low thermal conductivity of ATMS lead to the highest  $ZT$  in the AgMn<sub>m</sub>SbTe<sub>m+2</sub> system, which is ~0.27 at 300 K and reaches a maximum of ~1.46 at 823 K, higher than those of MnTe ( $ZT_{\text{max}} \sim 0.6$  at 823 K) and AgSbTe<sub>2</sub> ( $ZT_{\text{max}} \sim 1.0$  at 673 K). Furthermore, the average  $ZT$  ( $ZT_{\text{avg}}$ ) (400–823 K) of ATMS is ~0.87, compared to ~0.2 for MnTe (400–823 K) and ~0.85 for AgSbTe<sub>2</sub> (400–723 K). Such a high average  $ZT$  is comparable to those of other well-known thermoelectric materials (e.g., SnSe,<sup>64</sup> SnTe,<sup>65</sup> and BiCuSeO<sup>66</sup>). In addition, the ATMS has a Vickers microhardness hardness of ~190 H<sub>V</sub> (see experimental section in the Supporting Information for details), which is higher than that of state-of-the-art thermoelectric materials,<sup>67</sup> including Bi<sub>2</sub>Te<sub>3</sub> (~64 H<sub>V</sub>), PbTe (~35 H<sub>V</sub>), PbSe (~59 H<sub>V</sub>), Cu<sub>2</sub>S (~92 H<sub>V</sub>), GeTe (~145 H<sub>V</sub>). Such high thermoelectric performance and hardness imply that AgMnSbTe<sub>3</sub> should be

practically useful for mid-temperature thermoelectric applications.

## CONCLUDING REMARKS

This study proposes a new route to achieve cubic MnTe through entropy-driven alloying of AgSbTe<sub>2</sub> and reveals a promising  $p$ -type thermoelectric material, AgMnSbTe<sub>3</sub> (ATMS, i.e., equimolar mixture of AgSbTe<sub>2</sub> and MnTe). Our phase and microstructure analyses revealed that ATMS was composed of AgMnSbTe<sub>3</sub> and Ag<sub>2</sub>Te compounds, where AgMnSbTe<sub>3</sub> exhibited a rock-salt crystal structure with Ag, Mn, and Sb cooccupying the Na sites and had local lattice distortion. In addition, AgMnSbTe<sub>3</sub> is a narrow-band-gap semiconductor with an optical band gap of ~0.3 eV and has a specific multiple valence band structure with a low energy separation between the top three VBMs. Ag<sub>2</sub>Te with an amount of 3 mol% was distributed at the boundaries of the AgMnSbTe<sub>3</sub> grains, which acted as transmission channels for holes in ATMS. As a consequence, ATMS exhibited better electrical and thermal transport properties than those of pristine MnTe and AgSbTe<sub>2</sub>, which provided an ultralow lattice thermal conductivity of ~0.34  $\text{Wm}^{-1}\text{K}^{-1}$  at 823 K, peak  $ZT$  of ~1.46 at 823 K, and high average power factor of ~8.5  $\mu\text{Wcm}^{-1}\text{K}^{-2}$  and average  $ZT$  of 0.87 in the temperature range of 400–823 K. This shows the high potential of the lead-free ATMS for medium-temperature thermoelectric power generators.

## ASSOCIATED CONTENT

### Supporting Information

Experimental and computational details, including Hall carrier concentration and mobility, thermal properties, sound velocity, ultraviolet photoelectron spectroscopy spectra, Vickers microhardness and Fourier transform infrared spectrum.

## AUTHOR INFORMATION

### Corresponding Author

\* Junyou Yang

State Key Laboratory of Materials Processing and Die & Mold Technology, Huazhong University of Science and Technology, Wuhan, 430074, P. R. China

Email: jy yang@mail.hust.edu.cn

\* Qingyu Yan

School of Materials Science and Engineering, Nanyang Technological University, 50 Nanyang Avenue, Singapore 639798, Singapore.

Email: AlexYan@ntu.edu.sg

\* Mercouri G. Kanatzidis

Department of Chemistry, Northwestern University, Evanston, Illinois 60208, USA.

Email: m-kanatzidis@northwestern.edu

### Notes

The authors declare no competing financial interest.

## ■ ACKNOWLEDGMENT

This study was supported by the Department of Energy, Office of Science, Basic Energy Sciences under grant DE-SC0014520, DOE Office of Science (sample preparation, synthesis, XRD, thermoelectric measurements, TEM measurements, DFT calculations). The User Facilities are supported by the Office of Science of the U.S. Department of Energy under Contract Nos. DE-AC02-06CH11357 and DE-AC02-05CH11231. We acknowledge the access to facilities for high-performance computations at Northwestern University, Singapore MOE AcRF Tier 2 under Grant No. 2018-T2-1-010, Singapore A\*STAR Pharos Program SERC 1527200022, Singapore A\*STAR project A19D9a0096, support from FACTs of Nanyang Technological University for the sample analysis, National Natural Science Foundation of China (Grant Nos. 52002137, 51802070, 51572098, and 51632006), National Basic Research Program of China (Grant No. 2013CB632500), the Fundamental Research Funds for the Central Universities under Grant No. 2021XXJS008 and 2018KFYXKJC002, Natural Science Foundation of Hubei Province (Grant No. 2015CFB432), Open Fund of State Key Laboratory of Advanced Technology for Materials Synthesis and Processing, Wuhan University of Technology (No. 2016-KF-5), and Graduates' Innovation Fund, Huazhong University of Science and Technology (No. 2019ygsxcxy032). We gratefully acknowledge the technical assistance from the Analytical and Testing Center of HUST.

## ■ REFERENCES

- (1) He, J.; Tritt, T. M., Advances in thermoelectric materials research: Looking back and moving forward. *Science* **2017**, 357 (6358).
- (2) Tan, G.; Ohta, M.; Kanatzidis, M. G., Thermoelectric power generation: from new materials to devices. *Philos. Trans. A, Math. Phys. Eng. Sci.* **2019**, 377, 20180450.
- (3) Meroz, O.; Ayoun, D. B.; Beeri, O.; Gelbstein, Y., Development of  $\text{Bi}_2\text{Te}_{2.4}\text{Se}_{0.6}$  Alloy for Thermoelectric Power Generation Applications. *J. Alloys Compd.* **2016**, 679, 196.
- (4) Ayoun, D. B.; Sadia, Y.; Gelbstein, Y., High temperature thermoelectric properties evolution of  $\text{Pb}_{1-x}\text{Sn}_x\text{Te}$  based alloys. *J. Alloys Compd.* **2017**, 722, 33.
- (5) Jood, P.; Ohta, M.; Yamamoto, A.; Kanatzidis, M. G., Excessively doped PbTe with Ge-induced nanostructures enables high-efficiency thermoelectric modules. *Joule* **2018**, 2 (7), 1339-1355.
- (6) Liu, W.; Yin, K.; Zhang, Q.; Uher, C.; Tang, X., Eco-friendly high-performance silicide thermoelectric materials. *Natl. Sci. Rev.* **2017**, 4 (4), 611.
- (7) Goyal, G. K.; Dasgupta, T., Fabrication and testing of  $\text{Mg}_2\text{Si}_{1-x}\text{Sn}_x$  based thermoelectric generator module. *Mater. Sci. Eng. B.* **2021**, 272, 115338.
- (8) Kang, H. B.; Saparamadu, U.; Nozariasbmarz, A.; Li, W.; Zhu, H.; Poudel, B.; Priya, S., Understanding Oxidation Resistance of Half-Heusler Alloys for in-Air High Temperature Sustainable Thermoelectric Generators. *ACS Appl. Mater. Interfaces* **2020**, 12 (32), 36706.
- (9) Madar, N.; Givon, G.; Mogilyansky, D.; Gelbstein, Y., High thermoelectric potential of  $\text{Bi}_2\text{Te}_3$  alloyed GeTe-rich phases. *J. Appl. Phys.* **2016**, 120, 035102.
- (10) Tan, G.; Shi, F.; Hao, S.; Zhao, L.-D.; Chi, H.; Zhang, X.; Uher, C.; Wolverton, C.; Dravid, V. P.; Kanatzidis, M. G., Non-equilibrium processing leads to record high thermoelectric figure of merit in  $\text{PbTe-SrTe}$ . *Nat. Commun.* **2016**, 7, 12167.
- (11) Zhou, C.; Lee, Y. K.; Cha, J.; Yoo, B.; Cho, S.-P.; Hyeon, T.; Chung, I., Defect engineering for high-performance n-type PbSe thermoelectrics. *J. Am. Chem. Soc.* **2018**, 140 (29), 9282-9290.
- (12) Perumal, S.; Samanta, M.; Ghosh, T.; Shenoy, U. S.; Bohra, A. K.; Bhattacharya, S.; Singh, A.; Waghmare, U. V.; Biswas, K., Realization of high thermoelectric figure of merit in GeTe by complementary co-doping of Bi and In. *Joule* **2019**, 3 (10), 2565-2580.
- (13) Xing, T.; Song, Q.; Qiu, P.; Zhang, Q.; Xia, X.; Liao, J.; Liu, R.; Huang, H.; Yang, J.; Bai, S., Superior performance and high service stability for GeTe-based thermoelectric compounds. *Natl. Sci. Rev.* **2019**, 6 (5), 944-954.
- (14) Hong, M.; Chen, Z. G.; Yang, L.; Liao, Z. M.; Zou, Y. C.; Chen, Y. H.; Matsumura, S.; Zou, J., Achieving  $zT > 2$  in p-Type  $\text{AgSbTe}_{2-x}\text{Se}_x$  Alloys via Exploring the Extra Light Valence Band and Introducing Dense Stacking Faults. *Adv. Energy. Mater.* **2018**, 8 (9), 1702333.
- (15) Roychowdhury, S.; Ghosh, T.; Arora, R.; Samanta, M.; Xie, L.; Singh, N. K.; Soni, A.; He, J.; Waghmare, U. V.; Biswas, K., Enhanced atomic ordering leads to high thermoelectric performance in  $\text{AgSbTe}_2$ . *Science* **2021**, 371 (6530), 722-727.
- (16) Nunna, R.; Qiu, P.; Yin, M.; Chen, H.; Hanus, R.; Song, Q.; Zhang, T.; Chou, M.-Y.; Agne, M. T.; He, J., Ultrahigh thermoelectric performance in  $\text{Cu}_2\text{Se}$ -based hybrid materials with highly dispersed molecular CNTs. *Energy Environ. Sci.* **2017**, 10 (9), 1928-1935.
- (17) Lee, Y. K.; Luo, Z.; Cho, S. P.; Kanatzidis, M. G.; Chung, I., Surface oxide removal for polycrystalline SnSe reveals near-single-crystal thermoelectric performance. *Joule* **2019**, 3 (3), 719-731.
- (18) Zhao, L.-D.; Lo, S.-H.; Zhang, Y.; Sun, H.; Tan, G.; Uher, C.; Wolverton, C.; Dravid, V. P.; Kanatzidis, M. G., Ultralow thermal conductivity and high thermoelectric figure of merit in SnSe crystals. *Nature* **2014**, 508 (7496), 373-377.
- (19) Zhao, L.-D.; Tan, G.; Hao, S.; He, J.; Pei, Y.; Chi, H.; Wang, H.; Gong, S.; Xu, H.; Dravid, V. P., Ultrahigh power factor and thermoelectric performance in hole-doped single-crystal SnSe. *Science* **2016**, 351 (6269), 141-144.
- (20) Luo, Y.; Yang, J.; Jiang, Q.; Li, W.; Zhang, D.; Zhou, Z.; Cheng, Y.; Ren, Y.; He, X., Progressive regulation of electrical and thermal transport properties to high-performance  $\text{CuInTe}_2$  thermoelectric materials. *Adv. Energy. Mater.* **2016**, 6 (12), 1600007.
- (21) Xie, H.; Hao, S.; Cai, S.; Bailey, T. P.; Uher, C.; Wolverton, C.; Dravid, V. P.; Kanatzidis, M. G., Ultralow thermal conductivity in diamondoid lattices: high thermoelectric performance in chalcopyrite  $\text{Cu}_{0.8+y}\text{Ag}_{0.2}\text{In}_{1-y}\text{Te}_2$ . *Energy Environ. Sci.* **2020**, 13 (10), 3693-3705.
- (22) Fu, C.; Bai, S.; Liu, Y.; Tang, Y.; Chen, L.; Zhao, X.; Zhu, T., Realizing high figure of merit in heavy-band p-type half-Heusler thermoelectric materials. *Nat. Commun.* **2015**, 6 (1), 1-7.
- (23) Liu, R.; Chen, H.; Zhao, K.; Qin, Y.; Jiang, B.; Zhang, T.; Sha, G.; Shi, X.; Uher, C.; Zhang, W., Entropy as a gene-like performance indicator promoting thermoelectric materials. *Adv. Mater.* **2017**, 29 (38), 1702712.

- (24) Jiang, B.; Yu, Y.; Cui, J.; Liu, X.; Xie, L.; Liao, J.; Zhang, Q.; Huang, Y.; Ning, S.; Jia, B., High-entropy-stabilized chalcogenides with high thermoelectric performance. *Science* **2021**, 371 (6531), 830-834.
- (25) Roychowdhury, S.; Ghosh, T.; Arora, R.; Waghmare, U. V.; Biswas, K., Stabilizing n-Type Cubic GeSe by Entropy-Driven Alloying of AgBiSe<sub>2</sub>: Ultralow Thermal Conductivity and Promising Thermoelectric Performance. *Angew. Chem. Int. Ed. Engl.* **2018**, 130 (46), 15387-15391.
- (26) Wang, H.-X.; Mao, L.-S.; Tan, X.; Liu, G.-Q.; Xu, J.; Shao, H.; Hu, H.; Jiang, J., Nontrivial thermoelectric behavior in cubic SnSe driven by spin-orbit coupling. *Nano Energy* **2018**, 51, 649-655.
- (27) Samanta, M.; Ghosh, T.; Arora, R.; Waghmare, U. V.; Biswas, K., Realization of both n-and p-type GeTe thermoelectrics: electronic structure modulation by AgBiSe<sub>2</sub> alloying. *J. Am. Chem. Soc.* **2019**, 141 (49), 19505-19512.
- (28) Luo, Y.; Hao, S.; Cai, S.; Slade, T. J.; Luo, Z. z.; Dravid, V. P.; Wolverton, C.; Yan, Q.; Kanatzidis, M. G., High Thermoelectric Performance in the New Cubic Semiconductor AgSnSbSe<sub>3</sub> by High Entropy Engineering. *J. Am. Chem. Soc.* **2020**, 142 (35), 15187-15198.
- (29) Hu, L.; Zhang, Y.; Wu, H.; Li, J.; Li, Y.; McKenna, M.; He, J.; Liu, F.; Pennycook, S. J.; Zeng, X., Entropy Engineering of SnTe: Multi-Principal-Element Alloying Leading to Ultralow Lattice Thermal Conductivity and State-of-the-Art Thermoelectric Performance. *Adv. Energy Mater.* **2018**, 8 (29), 1802116.
- (30) Qiu, Y.; Jin, Y.; Wang, D.; Guan, M.; He, W.; Peng, S.; Liu, R.; Gao, X.; Zhao, L.-D., Realizing high thermoelectric performance in GeTe through decreasing the phase transition temperature via entropy engineering. *J. Mater. Chem. A* **2019**, 7 (46), 26393-26401.
- (31) Xin, J.; Yang, J.; Jiang, Q.; Li, S.; Basit, A.; Hu, H.; Long, Q.; Li, S.; Li, X., Reinforced bond covalency and multiscale hierarchical architecture to high performance eco-friendly MnTe-based thermoelectric materials. *Nano Energy* **2019**, 57, 703-710.
- (32) Xu, Y.; Li, W.; Wang, C.; Li, J.; Chen, Z.; Lin, S.; Chen, Y.; Pei, Y., Performance optimization and single parabolic band behavior of thermoelectric MnTe. *J. Mater. Chem. A* **2017**, 5 (36), 19143-19150.
- (33) Dong, J.; Wu, C.-F.; Pei, J.; Sun, F.-H.; Pan, Y.; Zhang, B.-P.; Tang, H.; Li, J.-F., Lead-free MnTe mid-temperature thermoelectric materials: facile synthesis, p-type doping and transport properties. *J. Mater. Chem. C* **2018**, 6 (15), 4265-4272.
- (34) Ren, Y.; Jiang, Q.; Yang, J.; Luo, Y.; Zhang, D.; Cheng, Y.; Zhou, Z., Enhanced thermoelectric performance of MnTe via Cu doping with optimized carrier concentration. *J. Materiomics* **2016**, 2 (2), 172-178.
- (35) Zheng, Y.; Lu, T.; Polash, M. M.; Rasoulianboroujeni, M.; Liu, N.; Manley, M. E.; Deng, Y.; Sun, P.; Chen, X.; Hermann, R. P., Paramagnon drag in high thermoelectric figure of merit Li-doped MnTe. *Sci. Adv.* **2019**, 5 (9), eaat9461.
- (36) Ren, Y.; Yang, J.; Jiang, Q.; Zhang, D.; Zhou, Z.; Li, X.; Xin, J.; He, X., Synergistic effect by Na doping and S substitution for high thermoelectric performance of p-type MnTe. *J. Mater. Chem. C* **2017**, 5 (21), 5076-5082.
- (37) Deng, H.; Lou, X.; Lu, W.; Zhang, J.; Li, D.; Li, S.; Zhang, Q.; Zhang, X.; Chen, X.; Zhang, D., Realizing ultrahigh performance in eco-friendly MnTe thermoelectrics by manipulating band structure and introducing SnTe nanocrystals. *Nano Energy* **2020**, 73, 104832.
- (38) Dong, J.; Pei, J.; Hayashi, K.; Saito, W.; Li, H.; Cai, B.; Miyazaki, Y.; Li, J.-F., Enhanced thermoelectric performance in MnTe due to doping and in-situ nanocompositing effects by Ag<sub>2</sub>S addition. *J. Materiomics* **2020**, 7 (3), 577-584.
- (39) Zaferani, S. H.; Ghomashchi, R.; Vashae, D., Thermoelectric, Magnetic, and Mechanical Characteristics of Antiferromagnetic Manganese Telluride Reinforced with Graphene Nanoplates. *Adv. Eng. Mater.* **2021**, 23 (2), 2000816.
- (40) Basit, A.; Yang, J.; Jiang, Q.; Xin, J.; Li, X.; Li, S.; Li, S.; Long, Q., Simultaneous regulation of electrical and thermal transport properties in MnTe chalcogenides via the incorporation of p-type Sb<sub>2</sub>Te<sub>3</sub>. *J. Mater. Chem. A* **2018**, 6, 23473.
- (41) Janik, E.; Dynowska, E.; Bak-Misiuk, J.; Leszczyński, M.; Szuszkiewicz, W.; Wojtowicz, T.; Karczewski, G.; Zakrzewski, A.; Kossut, J., Structural properties of cubic MnTe layers grown by MBE. *Thin Solid Films* **1995**, 267 (1), 74-78.
- (42) Griffiths, C. H., Cubic manganous telluride. *J. Mater. Sci.* **1978**, 13, 513.
- (43) Quarez, E.; Hsu, K.-F.; Pcionek, R.; Frangis, N.; Polychroniadis, E.; Kanatzidis, M. G., Nanostructuring, compositional fluctuations, and atomic ordering in the thermoelectric materials AgPb<sub>m</sub>SbTe<sub>2+m</sub>. The myth of solid solutions. *J. Am. Chem. Soc.* **2005**, 127 (25), 9177-9190.
- (44) Xu, J.; Li, H.; Du, B.; Tang, X.; Zhang, Q.; Uher, C., High thermoelectric figure of merit and nanostructuring in bulk AgSbTe<sub>2</sub>. *J. Mater. Chem.* **2010**, 20 (29), 6138-6143.
- (45) Wu, H.-j.; Chen, S.-w.; Ikeda, T.; Snyder, G. J., Reduced thermal conductivity in Pb-alloyed AgSbTe<sub>2</sub> thermoelectric materials. *Acta Mater.* **2012**, 60 (17), 6144-6151.
- (46) Banik, A.; Ghosh, T.; Arora, R.; Dutta, M.; Pandey, J.; Acharya, S.; Soni, A.; Waghmare, U. V.; Biswas, K., Engineering ferroelectric instability to achieve ultralow thermal conductivity and high thermoelectric performance in Sn<sub>1-x</sub>Ge<sub>x</sub>Te. *Energy Environ. Sci.* **2019**, 12 (2), 589-595.
- (47) Dutta, M.; Pal, K.; Waghmare, U. V.; Biswas, K., Bonding heterogeneity and lone pair induced anharmonicity resulted in ultralow thermal conductivity and promising thermoelectric properties in n-type AgPbBiSe<sub>3</sub>. *Chem. Sci.* **2019**, 10 (18), 4905-4913.
- (48) Shamoto, S.; Yamada, N.; Matsunaga, T.; Proffen, T.; Richardson, J.; Chung, J.-H.; Egami, T., Large displacement of germanium atoms in crystalline Ge<sub>2</sub>Sb<sub>2</sub>Te<sub>5</sub>. *Appl. Phys. Lett.* **2005**, 86 (8), 081904.
- (49) Cai, S.; Hao, S.; Luo, Z.-Z.; Li, X.; Hadar, I.; Bailey, T. P.; Hu, X.; Uher, C.; Hu, Y.-Y.; Wolverton, C., Discordant nature of Cd in PbSe: off-centering and core-shell nanoscale CdSe precipitates lead to high thermoelectric performance. *Energy Environ. Sci.* **2020**, 13 (1), 200-211.
- (50) Luo, Z. Z.; Cai, S.; Hao, S.; Bailey, T. P.; Spanopoulos, I.; Luo, Y.; Xu, J.; Uher, C.; Wolverton, C.; Dravid, V. P., Strong Valence Band Convergence to Enhance Thermoelectric Performance in PbSe with Two Chemically Independent Controls. *Angew. Chem. Int. Ed. Engl.* **2021**, 133 (1), 272-277.
- (51) Scanlon, D. O.; Walsh, A., Bandgap engineering of ZnSnP<sub>2</sub> for high-efficiency solar cells. *Appl. Phys. Lett.* **2012**, 100 (25), 251911.
- (52) Ektarawong, A.; Simak, S.; Hultman, L.; Birch, J.; Alling, B., First-principles study of configurational disorder in B<sub>4</sub>C using a superatom-special quasirandom structure method. *Phys. Rev. B* **2014**, 90 (2), 024204.
- (53) Zhang, J.; Su, C.; Liu, Y., First-principles study of bcc Fe-

- Cr-Si binary and ternary random alloys from special quasi-random structure. *Physica. B, Condensed matter*. **2020**, 586, 412085.
- (54) Söderlind, P.; Zhou, F.; Landa, A.; Klepeis, J., Phonon and magnetic structure in  $\delta$ -plutonium from density-functional theory. *Sci. Rep.* **2015**, 5 (1), 1-6.
- (55) Tian, F., A Review of Solid-Solution Models of High-Entropy Alloys Based on Ab Initio Calculations. *Front. Mater.* **2017**, 4, 36
- (56) Kim, H.-S.; Heinz, N. A.; Gibbs, Z. M.; Tang, Y.; Kang, S. D.; Snyder, G. J., High thermoelectric performance in  $(\text{Bi}_{0.25}\text{Sb}_{0.75})_2\text{Te}_3$  due to band convergence and improved by carrier concentration control. *Mater. Today* **2017**, 20 (8), 452-459.
- (57) Slade, T. J.; Bailey, T. P.; Grovogui, J. A.; Hua, X.; Zhang, X.; Kuo, J. J.; Hadar, I.; Snyder, G. J.; Wolverton, C.; Dravid, V. P., High thermoelectric performance in  $\text{PbSe-NaSbSe}_2$  alloys from valence band convergence and low thermal conductivity. *Adv. Energy Mater.* **2019**, 9 (30), 1901377.
- (58) Goldsmid, H.; Sharp, J. W., Estimation of the thermal band gap of a semiconductor from seebeck measurements. *J. Electron. Mater.* **1999**, 28, 869.
- (59) Kim, H.-S.; Gibbs, Z. M.; Tang, Y.; Wang, H.; Snyder, G. J., Characterization of Lorenz number with Seebeck coefficient measurement. *APL Mater.* **2015**, 3 (4), 041506.
- (60) Jana, M. K.; Pal, K.; Waghmare, U. V.; Biswas, K., The Origin of Ultralow Thermal Conductivity in  $\text{InTe}$ : Lone-Pair-Induced Anharmonic Rattling. *Angew. Chem. Int. Ed. Engl.* **2016**, 128 (27), 7923-7927.
- (61) Tak, J.-Y.; Nam, W. H.; Lee, C.; Kim, S.; Lim, Y. S.; Ko, K.; Lee, S.; Seo, W.-S.; Cho, H. K.; Shim, J.-H., Ultralow lattice thermal conductivity and significantly enhanced near-room-temperature thermoelectric figure of merit in  $\alpha\text{-Cu}_2\text{Se}$  through suppressed Cu vacancy formation by overstoichiometric Cu addition. *Chem. Mater.* **2018**, 30 (10), 3276-3284.
- (62) Luo, Y.; Cai, S.; Hua, X.; Chen, H.; Liang, Q.; Du, C.; Zheng, Y.; Shen, J.; Xu, J.; Wolverton, C., High Thermoelectric Performance in Polycrystalline  $\text{SnSe}$  Via Dual-Doping with Ag/Na and Nanostructuring with  $\text{Ag}_8\text{SnSe}_6$ . *Adv. Energy Mater.* **2019**, 9 (2), 1803072.
- (63) Li, W.; Lin, S.; Ge, B.; Yang, J.; Zhang, W.; Pei, Y., Low sound velocity contributing to the high thermoelectric performance of  $\text{Ag}_8\text{SnSe}_6$ . *Adv. Sci.* **2016**, 3 (11), 1600196.
- (64) Chen, Z.-G.; Shi, X.; Zhao, L.-D.; Zou, J., High-performance  $\text{SnSe}$  thermoelectric materials: Progress and future challenge. *Prog. Mater. Sci.* **2018**, 97, 283-346.
- (65) Tan, G.; Hao, S.; Hanus, R. C.; Zhang, X.; Anand, S.; Bailey, T. P.; Rettie, A. J.; Su, X.; Uher, C.; Dravid, V. P., High Thermoelectric Performance in  $\text{SnTe-AgSbTe}_2$  Alloys from Lattice Softening, Giant Phonon-Vacancy Scattering, and Valence Band Convergence. *ACS Energy Lett.* **2018**, 3 (3), 705-712.
- (66) Lan, J. L.; Liu, Y. C.; Zhan, B.; Lin, Y. H.; Zhang, B.; Yuan, X.; Zhang, W.; Xu, W.; Nan, C. W., Enhanced thermoelectric properties of Pb-doped  $\text{BiCuSeO}$  ceramics. *Adv. Mater.* **2013**, 25 (36), 5086-5090.
- (67) Suwardi, A.; Lim, S. H.; Zheng, Y.; Wang, X.; Chien, S. W.; Tan, X. Y.; Zhu, Q.; Wong, L. M. N.; Cao, J.; Wang, W.; Yan, Q.; Tan, C. K. I.; Xu, J., Effective enhancement of thermoelectric and mechanical properties of germanium telluride via rhenium-doping. *J. Mater. Chem. C* **2020**, 8, 16940.

---

## Figure captions

**Figure 1. Crystal structure of AgMnSbTe<sub>3</sub>.** (A) Powder X-ray diffraction (XRD) patterns of MnTe and AgMn<sub>m</sub>SbTe<sub>m+2</sub>, (m=1, 2, 4, 6 and 10). (B) Rietveld refinement of the powder XRD pattern of m=1 sample (ATMS). (C) Long r region fit using disordered cubic AgMnSbTe<sub>3</sub> (Figure S1). (D) Low r region fit using cubic disordered AgMnSbTe<sub>3</sub> (Figure S1). (E) Fitting crystal structure of distorted AgMnSbTe<sub>3</sub> with off-centered Ag atoms (cations red, anions blue) under P1 symmetry. (F) Low r region fit using distorted AgMnSbTe<sub>3</sub> (panel E).

**Figure 2. Microstructure of ATMS.** (A) Back-scattered electron image and (B) energy-dispersive X-ray spectroscopic analysis of points 1, 2, 3, 4 marked in panel A. (C) Scanning transmission electron microscopic (STEM) image and (D) EDS mapping for AgMnSbTe<sub>3</sub> grains. (E) transmission electron microscopic (TEM) image of ATMS, (F) high resolution TEM image of the area marked in panel E, the inset of panel F is the Fourier Fast Transform pattern of Ag<sub>2</sub>Te.

**Figure 3. Electronic profile of AgMnSbTe<sub>3</sub>.** Spin-polarized electronic band structure for AgMnSbTe<sub>3</sub> in spin up (A) and spin down (B). (C) Total density of state (DOS) for spin up and spin down channels of AgMnSbTe<sub>3</sub>, (D) orbital projected DOS for spin up and spin down channels of AgMnSbTe<sub>3</sub>. (E) Ultraviolet photoelectron spectroscopy spectra of AgMnSbTe<sub>3</sub> (blue curve) and Ag<sub>2</sub>Te (red curve). (F) Schematic diagram of the valence band alignment in ATMS.

**Figure 4. Thermoelectric performance of AgMn<sub>m</sub>SbTe<sub>m+2</sub> (m=1, 2, 4, 6 and 10).** Temperature dependent (A) electrical conductivities, (B) Seebeck coefficients, (C) power factors, (D) thermal conductivities, (E) lattice thermal conductivities and (F) figure of merit ZT values.



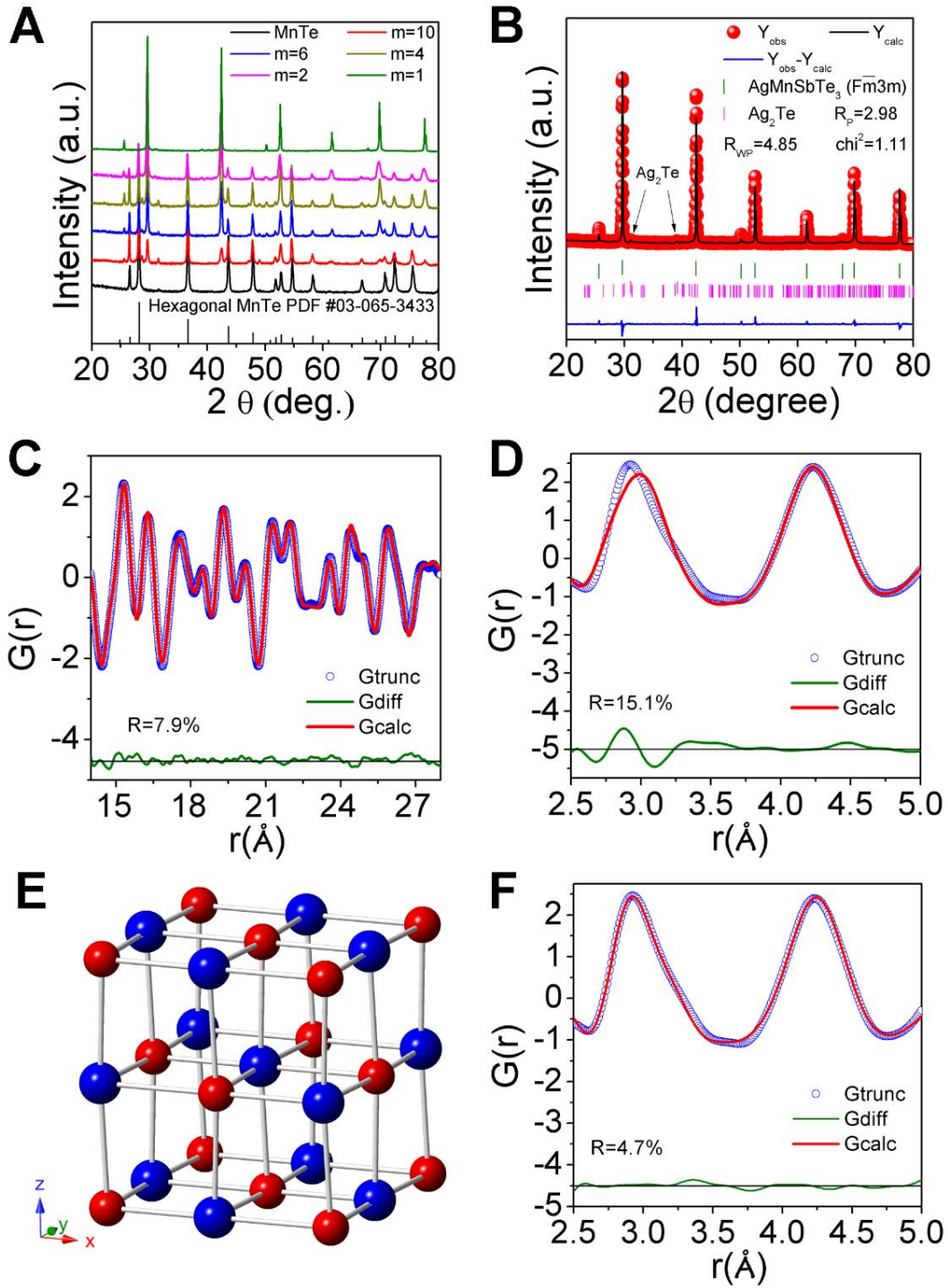


**Figure 1. Crystal structure of  $\text{AgMnSbTe}_3$ .** (A) Powder X-ray diffraction (XRD) patterns of  $\text{MnTe}$  and  $\text{AgMn}_m\text{SbTe}_{m+2}$  ( $m=1, 2, 4, 6$  and  $10$ ). (B) Rietveld refinement of the powder XRD pattern of  $m=1$  sample (ATMS). (C) Long  $r$  region fit using disordered cubic  $\text{AgMnSbTe}_3$  (Figure S1). (D) Low  $r$  region fit using cubic disordered  $\text{AgMnSbTe}_3$  (Figure S1). (E) Fitting crystal structure of distorted  $\text{AgMnSbTe}_3$  with off-centered Ag atoms (cations red, anions blue) under  $P1$  symmetry. (F) Low  $r$  region fit using distorted  $\text{AgMnSbTe}_3$  (panel E).

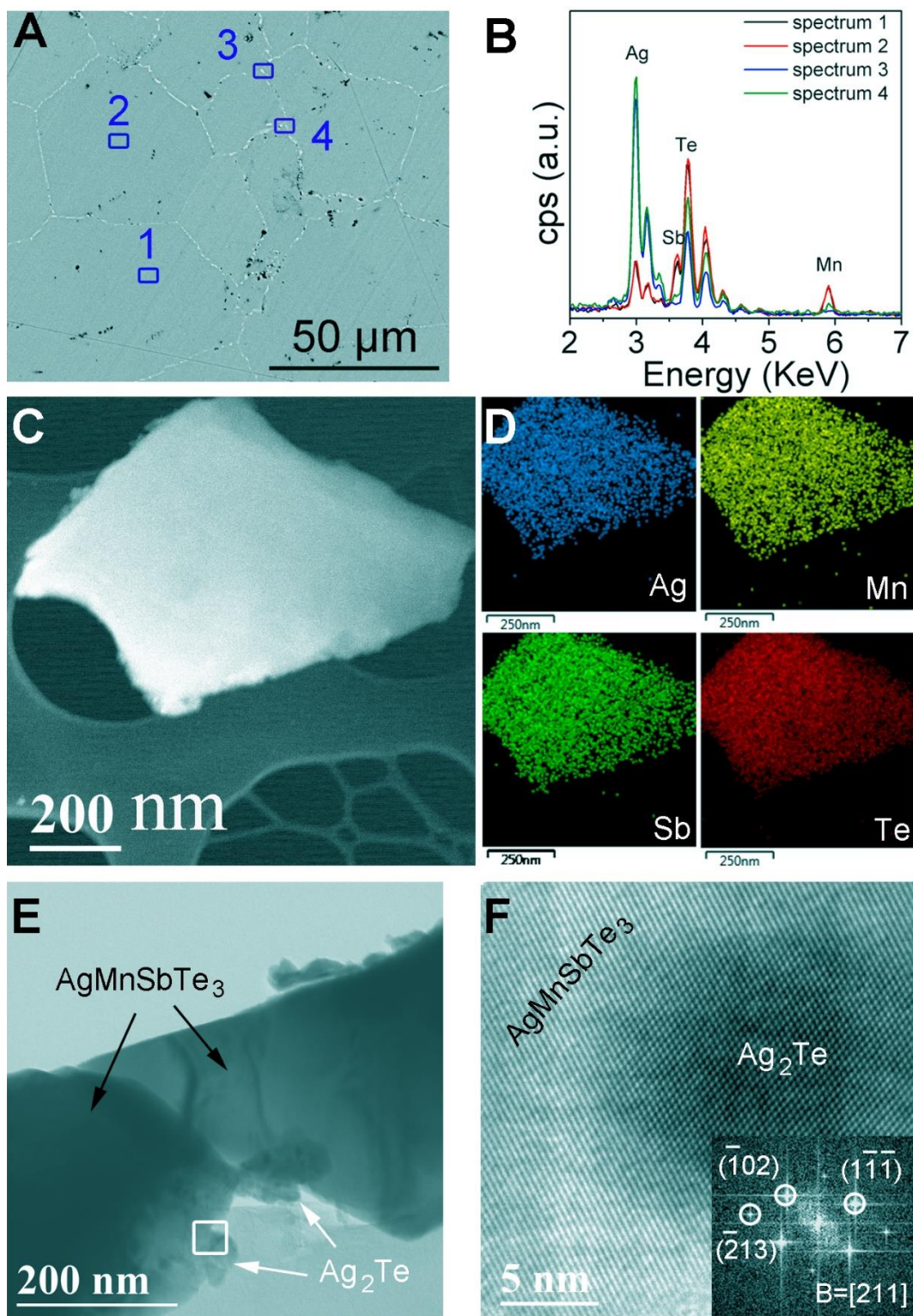


**Figure 2. Microstructure of ATMS.** (A) Back-scattered electron image and (B) energy-dispersive X-ray spectroscopic analysis of points 1, 2, 3, 4 marked in panel A. (C) Scanning transmission electron microscopic (STEM) image and (D) EDS mapping for  $\text{AgMnSbTe}_3$  grains. (E) transmission electron microscopic (TEM) image of ATMS, (F) high resolution TEM image of the area marked in panel E, the inset of panel F is the Fourier Fast Transform pattern of  $\text{Ag}_2\text{Te}$ .

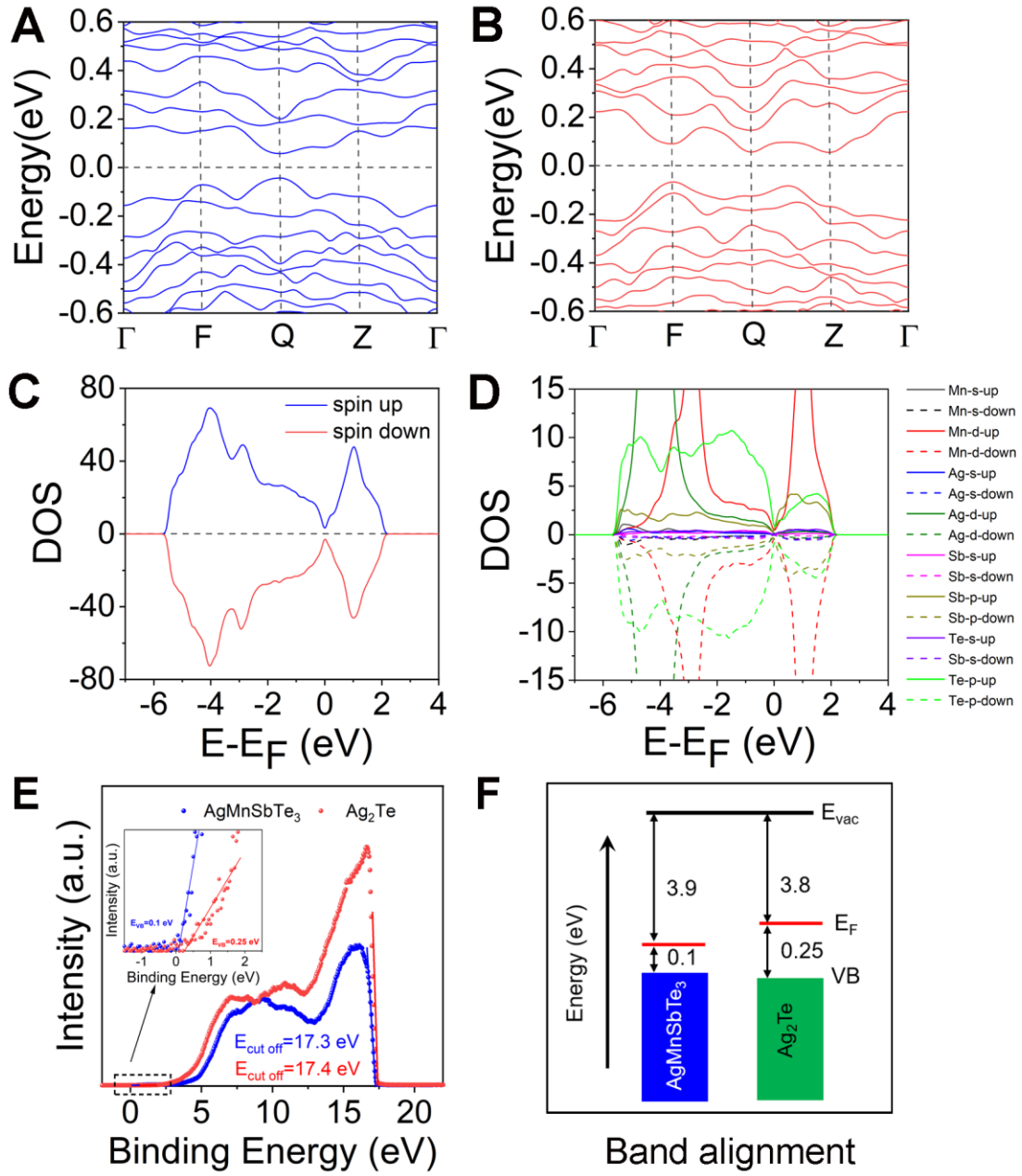


**Figure 3. Electronic profile of AgMnSbTe<sub>3</sub>.** Spin-polarized electronic band structure for AgMnSbTe<sub>3</sub> in spin up (A) and spin down (B). (C) Total density of state (DOS) for spin up and spin down channels of AgMnSbTe<sub>3</sub>, (D) orbital projected DOS for spin up and spin down channels of AgMnSbTe<sub>3</sub>. (E) Ultraviolet photoelectron spectroscopy spectra of AgMnSbTe<sub>3</sub> (blue curve) and Ag<sub>2</sub>Te (red curve). (F) Schematic diagram of the valence band alignment in ATMS.



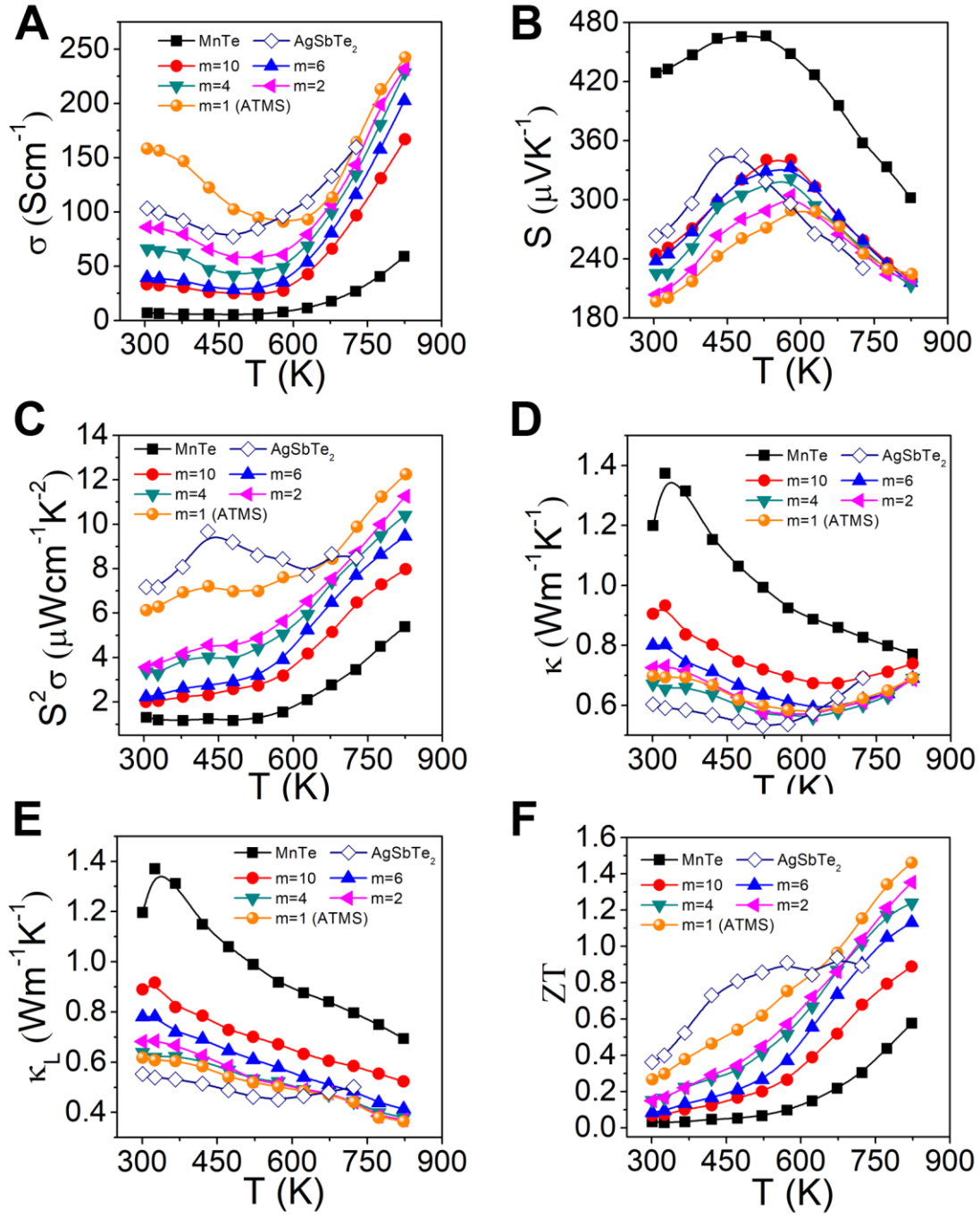


**Figure 4. Thermoelectric performance of  $\text{AgMn}_m\text{SbTe}_{m+2}$  ( $m=1, 2, 4, 6$  and  $10$ ).** Temperature dependent (A) electrical conductivities, (B) Seebeck coefficients, (C) power factors, (D) thermal conductivities, (E) lattice thermal conductivities and (F) figure of merit  $ZT$  values.



## TOC Graphic

